MSEC2020-8259

SEMICONDUCTOR ASPECTS OF THE OXYFUEL CUTTING TORCH PREHEAT FLAME PART II: THE FLAME'S INTERNAL ELECTRICAL STRUCTURE

Christopher R. Martin*
Teresa Pond
Jacob Tomas
Jenna Schmit
Erikson Miguel
Altoona College
Penn State Unviersity
Altoona, PA

Alex Untaroiu
Kemu Xu
Department of Mechanical Engineering
Virginia Tech
Blacksburg, VA

ABSTRACT

This two-part paper presents precise measurements of the ion currents passing between the torch and work piece of the preheat flame of an oxyfuel cutting torch as a means for replacing contemporary sensing suites. Part II presents the results of a novel spinning disc Langmuir probe technique to construct spatially resolved measurements of the flame's ion density distribution. A bias voltage is applied to a .254mm diameter wire protruding from a spinning disc, and as the wire is passed through the flame, the measured currents (on the order $10\mu A$) are collected. The process is repeated with incremental wire depths in the flame to construct the entire planar cross-sectional ion density. Measurements reveal intense ion concentrations in the inner cones that rapidly decay by an order of magnitude in the surrounding flow. The outer cone forms a hollow cylinder of weak ion concentration that declines with distance from the inner cones in a manner consistent with recombination.

1 Introduction

As we establish in part I of this paper [1], ion current measurements in the oxyfuel cutting flame are a promising technology to augment or replace the existing sensing suites for these

systems. These are small currents that can be made to pass between the torch and work piece through the flame. In part I, we present methods for scrutinizing aspects of the current-voltage characteristic between the torch and work piece to establish measures of standoff distance, ready-to-pierce, pierce success, cut health, loss-of-cut, and preheat flame health.

In this paper, we present a novel technique for spatially resolved measurements of ion density in the preheat flame. Our present approach to sensing rests on a number of presumptions about the spatial arrangement of ions inside the flame; where they are generated, how they migrate, and how saturation occurs. Before entrusting critical sensing tasks to such a technology, the underlying physics should be thoroughly understood; we begin that process here.

1.1 Previous ion density measurements in flames

Signal-level measurements of ion currents were a prominent part of Thompson's case for the existence of the electron [2] over a century ago. He and his contemporaries found that voltages between platinum wires in a flame could be made to drive electrical currents up to a maximum, which was called saturation. Langmuir famously demonstrated that a cylindrical or spherical probe could be used to study these plasmas [3], and Boucher and Banta were able to collect exquisitely precise measurements of the de-

^{*}Email: crm28@psu.edu

pletion of charge near a metal surface (now called a "sheath") using wire probes [4,5].

The study of ion concentrations in flames at atmospheric pressure is severely hindered by the temperatures involved and the efficiency of heat transfer to the probe. Spatially resolved measurements were used by Calcote in his study of the ion formation mechanisms [6], but his probe used an actively cooled platinum wire in sub-atmospheric pressures with air as the oxidizer. The density of atmospheric pressure flames drastically increases the rate heat transfer, and oxyfuel is used for metal working precisely because the flame temperature is far above the melting temperatures of most metals. Worse still, the geometric complexity of the oxyfuel preheat flame requires that the probe be quite small (we use .25mm or .010in diameter) and long (at least 10mm or .4in), so actively cooled probes have little hope of surviving.

Instead, we propose to inject a small wire into the flame for extremely short periods of time; long enough to collect an electrical measurement, but brief enough to ensure that the wire survives. It appears that the idea was first proposed by MacLatchy [7], who used a spinning disc with a wire mounted radially at its perimeter. The works of Clements and Smy on Langmuir probes in dense plasmas [8, 9, 10, 11] establish that the probe's saturation current density is a function of its diameter, the local fluid velocity, and the local ion density. If a wire is driven to negative voltages, electrons are driven away, and the measured current per unit length of wire is proportional to the density of positive molecules in the plasma.

1.2 Spatially resolved measurements

Unfortunately, for a wire injected into a plasma where ion density cannot be assumed constant along its length, currents at the wire's base may be very different from currents at the wire's tip. It is not possible to simply calculate an average along the wire length as was done by MacLatchy. How is it possible to make spatially resolved measurements? We draw inspiration from tomography and Abel transformation methods, which infer some spatially distributed property from a plurality of integrated line-of-sight measurements. In the same way, we extract spatially resolved current density measurements from a plurality of individual wire measurements.

We will present the details of the transformation in Section 3, but the approach may be understood by considering a current measurement obtained from a wire on a spinning disc that can be moved towards and away from the flame. When the disc is positioned so that only the very tip of the wire touches the flame and only the slightest current is detected, then no complicated transform is needed; all of the current was measured at the wire tip, and the ion density at the flame's edge may be inferred directly. If we were to move the disc so the wire is inserted more deeply, the signal will increase. If we scrutinize the rate of increase with

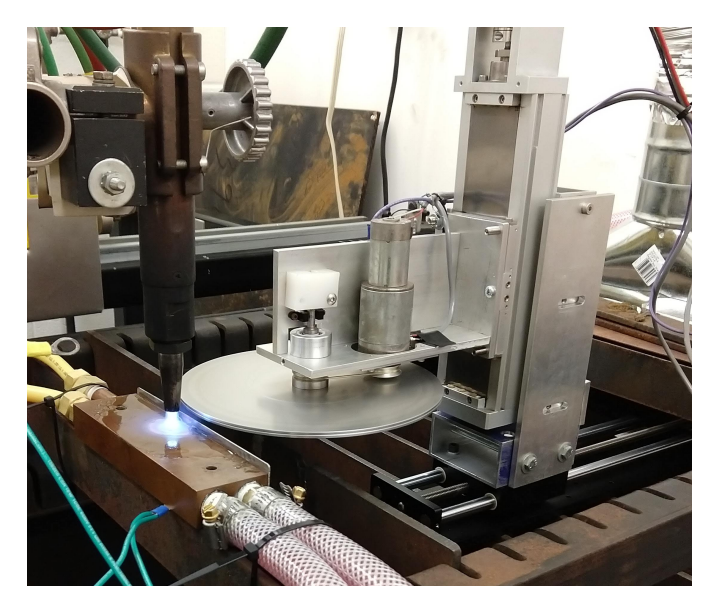


FIGURE 1. A photograph of the spinning-disc Langmuir probe in use.

great care, we might subtract off the current we already know to be encountered at the flame's edge, leaving only the new signal encountered at the wire's tip; now deeper in the flame. If this process is repeated throughout the flame's depth, an electrical cross-section of the flame can be constructed.

2 Experimental design

Two 203mm (8in) diameter aluminum discs capture a .254mm (.010in) diameter nichrome wire, which extends 25.4mm (1.00in) radially from the discs' edge. The discs are mounted on a steel spindle, which is, in turn, mounted in a pair of ceramic (ZrO₂) bearings lubricated with dielectric grease. The spindle is turned by a DC brush motor via a round urethane belt. The only electrically conductive connection to the spindle and disc is made through a spring-loaded gold-plated pin mounted in the white HDPE block visible above the spindle in Figure 1. Between the white block and the bearings, a photo-interrupter straddles the spindle and produces a pulse when a hole drilled in the shaft aligns with the device.

The preheat flame gas flow rates were monitored by thermal mass flow meters and metering valves in a separate room to protect from thermal drift typical of the torch's metering valves.

2.1 Wire current measurements

Figure 2 shows how the elements of the system were connected. For these experiments, an Acopian linear power supply was set to -20V and connected through a sensitive current measurement device (called the "isoshunt" here) to the disc. The

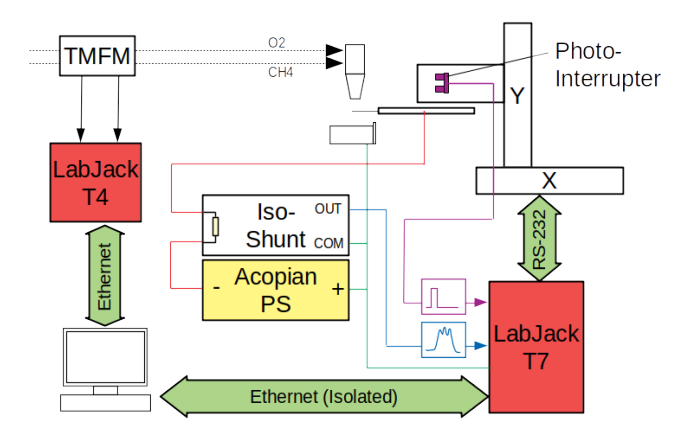


FIGURE 2. A system diagram of the experiment.

isoshunt created a voltage signal proportional to the current detected at the wire, which was then passed to a LabJack T7 data acquisition unit. The T7 recorded the optoisolator state and the wire current at 50kS/s throughout two-second tests.

The isoshunt circuit shown in Figure 3. This circuit directs the power supplied by the linear power supply through one side of a balanced bridge. When current flows to the wire, it unbalances the negative half of the bridge, causing a small differential signal at the input to a custom instrumentation amplifier. This arrangement allows for voltages at the power supply to be as low as -100V while still permitting highly sensitive measurements. This approach was necessary because attempts to place a shunt resistor between the power supply and ground caused severe 60Hz noise due to capacitive coupling through the transformer of the linear power supply. Grounding the power supply mitigates this issue.

The negative half of the bridge offers two means of connecting the experiment; a high-current connection for signals on the order of .1 to 10mA, and a low-current connection for signals on the order of 0.01 to $1\mu A$. The low-current connection was used for these experiments. Prior to each test, the zero was set to within 1mV. Then, a test current of $10\pm.01\mu A$ was driven through the measurement, and the gain was adjusted until a $5.000\pm.001V$ output was produced.

2.2 Scanning the flame

The entire probe assembly was mounted on vertical and horizontal translation stages visible in Figure 1. These allowed location of the experiment to within 0.1mm (.004in). To execute a scan of a horizontal plane of the flame, the vertical stage was located appropriately and the horizontal stage was used to dwell for two seconds at each of a series of horizontal locations. First, the disc was moved towards the flame in 0.25mm (.010in) increments to a 20mm depth before being retracted at the same incre-

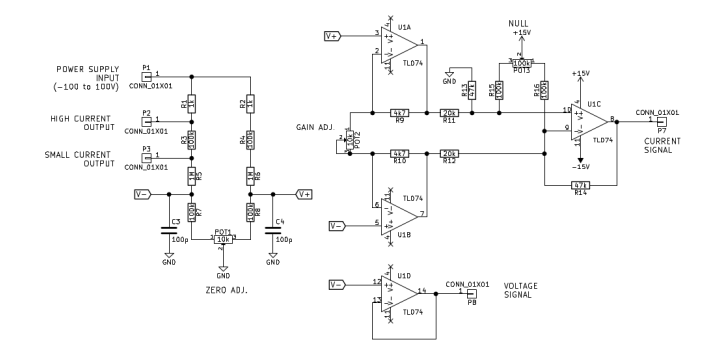


FIGURE 3. The precision isoshunt circuit used to measure wire current

ments, but with a 0.125mm (.005in) offset. In this way, each data set included 161 data sets spanning 20mm of disc displacement at 0.125mm increments, but with half of the data collected while inserting the wire and half of the data collected while extracting the wire.

Each data set consisted of two seconds of data collected while the disc was spinning at roughly 400rpm while the wire current signal and photointerrupter were sampled at 50kS/s. Of the resulting 100 thousand individual data points, only a small percentage were collected during the transit through the flame.

2.3 Disc speeds

Here, we devote some attention to ensuring the wire's survival in the flame. It spends the majority of its transit in ambient air, and only a short time in the intense heat of the flame. Still, when one simply injects a wire of the same material into the flame, it is not perceptible to the human eye that there is any delay before it begins to melt.

A wire of diameter, D_w , length, L, with specific heat, c, and density, ρ , undergoing convection with a coefficient, h, will heat according to the equation

$$\rho c \frac{L\pi D_w^2}{4} \dot{T} = \pi D_w Lh \left(T_{sur} - T \right).$$

This is a first-order system with time constant

$$\tau = \frac{\rho c D_w}{4h}.\tag{1}$$

Let us imagine that the wire enters the flame at time t = 0, and leaves the flame at time $t = t_f$, and travels a complete rotation at

time $t = t_c$. Let us define a dimensionless temperature,

$$k = \frac{T - T_{amb}}{T_{flame} - T_{amb}},\tag{2}$$

when T_{amb} is the ambient air temperature, and T_{flame} is the temperature in the flame. In this way, when k=0, the wire temperature is the same as the ambient, and when k=1, the wire temperature is at the flame temperature. Therefore, k obeys a simple piece-wise differential equation

$$\tau \dot{k} + k = \begin{cases} 1 : 0 \le t < t_f \\ 0 : t_f \le t < t_c \end{cases}$$
 (3)

If we imagine the wire's temperature to be k_{max} when leaving the flame and k_{min} just prior to entering the flame, we may solve the piecewise system to obtain

$$k(t) = \begin{cases} (k_{min} - 1) \exp(-t/\tau) + 1 : 0 \le t < t_f \\ k_{max} \exp(-(t - t_f)/\tau) : t_f \le t \le t_c \end{cases}$$
(4)

After the wire has made many journeys through the flame, the temperature of the wire entering the flame of one rotation is the same as the one prior. When we assert this continuity between at $k(0) = k(t_c)$ and $k(t_f^-) = k(t_f^+)$, we obtain an expression for the maximum and minimum temperatures purely in terms of the timing parameters.

$$k_{max} = \frac{1 - \exp(-t_f/\tau)}{1 - \exp(-t_c/\tau)}$$
 (5a)

$$k_{min} = \frac{\exp(-t_a/\tau) - \exp(-t_c/\tau)}{1 - \exp(-t_c/\tau)}$$
 (5b)

The times, t_c , t_a , and t_f , are determined by the rotation frequency, f and the fraction, $\chi = t_f/t_c$, of the disc's motion that places the wire in the flame.

$$t_c = \frac{1}{f}$$
 $t_f = \frac{\chi}{f}$ $t_a = \frac{1-\chi}{f}$

We may expand the exponentials of equation 5a to obtain a simpler estimate for the maximum temperature,

$$k_{max} \approx \chi \frac{2f\tau - \chi}{2f\tau - 1}.$$
(6)

Clearly, in the limit where $f\tau \gg 1$, $k_{max} \rightarrow \chi$.

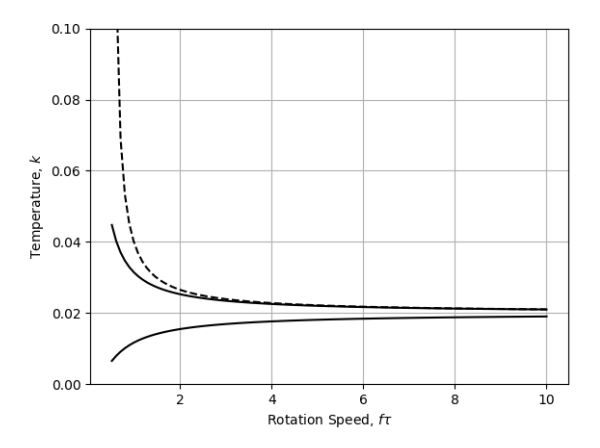


FIGURE 4. Maximum and minimum d-less temperatures versus d-less disc speed for $\chi = 0.2$. The dashed line is the approximate k_{max} from Equation 6

Figure 4 shows the dimensionless temperatures k_{max} and k_{min} versus disc speed, and the approximate k_{max} is plotted with a dashed line. The choice of $\chi = 0.02$ is consistent with a flame approximately 12mm (0.5in) across with a wire radius of 100mm (4in).

Nichrome steel enjoys a high mechanical strength, relatively high density (7,900 kg/m³), relatively high specific heat (500J/kg-K) and favorable resistance to corrosion. If the convective coefficient were approximated on the order of $1000W/m^2$ -K for a 0.25mm (0.01in) diameter wire, then the time constant, τ , of Equation 1 is about one quarter (0.25) seconds.

Since χ will be constant for a given flame and disc geometry, and k_{max} is a constraint based on the melting temperature of the wire, we may calculate a minimum safe disc speed. When we use the expansion in Equation 6, we will produce a conservative calculation for f that cannot be less than $1/2\tau$ due to the singularity in the expansion.

$$f > \left(\frac{1}{2\tau}\right) \left(\frac{k_{max} - \chi^2}{k_{max} - \chi}\right) \tag{7}$$

If the flame temperature were about 3000K, the wire melting temperature were about 1700K, and the ambient were about 300K, then $k_{max} = 0.52$, and the minimum disc speed is $f\tau > 0.52$. If τ is 0.25s, then the disc should spin at at least 2.1 rotations per second (124rpm).

For the present study we operate the disc at speeds near 7 revolutions per second (about 400rpm). These speeds are far in excess of what is required to protect a 0.25mm (.01in) diameter wire. If the wire tip is at a radius of 125mm (5in), it will travel at

roughly 5.3m/s (210in/s), which is safely less than the velocities that are likely in the flame.

The current signal that should be generated by such an experiment should form a pedestal with a width determined by the wire's duration in the flame, and with internal features determined by the length scale of the flame's micro-structures. If the wire processes with a speed of 5.3m/s (210in/s) through a 12mm (0.5in) flame, then the pedestal is approximately 2.3ms wide. The micro-structures that need to be resolved are probably determined by the number of individual flamelets formed at the tip's preheat openings. If we were to assume that these were so tightly spaced as 1mm, then the pedestal will contain features as fast as 0.2ms.

Time scales between 2.3ms and 0.2ms correspond to frequency content from 400Hz to 5kHz. Of course, these frequencies will scale with the disc speed. If these settings are respected, digital sampling must be *at least* 10kHz, and filtration below 5kHz must be avoided.

Were the diameter of the wire halved, so would the wire's thermal time constant, and the minimum disc speed would double. Because 400rpm was already an aggressive choice for a 0.25mm (.01in) wire, it should still be acceptable for a 0.12mm (.005in) diameter wire.

3 Post-processing

In post-processing, the raw wire current measurements must be aggregated and interpreted together in order to construct a map for where these currents occurred in space. The wire current density per unit area, $J_D(x,y)$, for a wire of diameter, D, may be taken as a property of the plasma at coordinates, x,y. The actual signal measured by the wire will be an integration of these local values all along the wire's length. The problem that we solve here is identifying values of J_D over the entire domain that minimize disagreement between direct measurement and calculated values of integrated wire currents.

We apply a coordinate system like the one shown in Figure 5. A wire with diameter, D_w , at an angle θ from the x-axis, extending a radius, R, from a center of rotation a distance, d, from the origin, will incur a current

$$I = \pi D_w \int_0^R J_D(r, d, \theta) dr$$
 (8)

when D_w is the wire diameter, and r is the distance along the wire.

We will estimate values of J_D at nodes with uniform spacing, δ , in both x and y directions. When we define a grid with N_x nodes along the x-axis and N_y nodes along the y-axis. The total

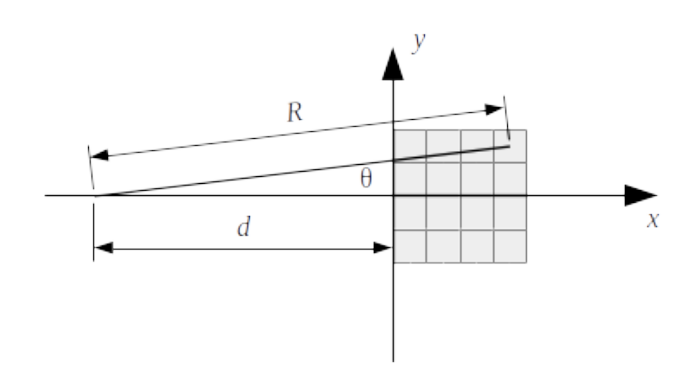


FIGURE 5. The coordinates used to locate the wire and grid nodes.

number of nodes, N_n and the number of square elements, N_e , are

$$N_n = N_x N_y \tag{9}$$

$$N_e = (N_x - 1)(N_y - 1). \tag{10}$$

If we were to arrange the values of J_D into a vector, \vec{X} , the integral in Equation 8 could be reduced to

$$I = \pi D_w \vec{\Lambda}(R, d, \theta) \cdot \vec{X}$$
 (11)

where each element of $\vec{\Lambda}$ quantifies the contribution of each node to the integral for a given wire location. While the details of how $\vec{\Lambda}$ should be calculated are beyond this paper, we offer a brief overview in the appendix. It may suffice to state that it is derived by applying a bilinear interpolation scheme between nodes to permit evaluation of the integral in Equation 8.

Unfortunately, this merely provides us a means for calculated wire current from a given current density field. In order to calculate \vec{X} from many hundreds (or thousands) of direct measurements of I with a wide variety of wire locations, we will develop a measure of error in our grid and seek to minimize it. A least-squares approach proves quite functional.

For the k^{th} measurement in a data set, the grid's error, e_k , will be

$$e_k = \pi D_w \vec{\Lambda}(R, d_k, \theta_k) \cdot \vec{X} - I_k \tag{12}$$

when I_k is the current measured with the disc location, d_k , and angle, $theta_k$. The total error from all measurements may be

assessed by the sum of squares, $E^2 = \sum_k e_k^2$. When our choices for the n^{th} element of \vec{X} is optimal,

$$0 = \frac{\partial E^2}{\partial X_n}$$

$$= 2\sum_{k} e_k \frac{\partial e_k}{X_n}$$

$$= 2\sum_{k} \left(\pi D_w \vec{\Lambda}(R, d_k, \theta_k) \cdot \vec{X} - I_k\right) \Lambda_n(R, d_k, \theta_k). \tag{13}$$

Here, Λ_n is the element of $\vec{\Lambda}$ corresponding to the n^{th} element of \vec{X} . We may simplify this into a single matrix equation by repeating it for each value of n to form a system of equations. For compactness, we also rewrite $\vec{\Lambda}(R, d_k, \theta_k) \cdot \vec{X}$ as $\vec{\Lambda}_k^{\ T} \vec{X}$. The result is simply

$$\frac{1}{\pi D_w} \sum_{k} \vec{\Lambda}_k I_k = \left[\sum_{k} \vec{\Lambda}_k \vec{\Lambda}_k^T \right] \vec{X}$$
 (14)

This represents a matrix inversion problem for the calculation of the node values, \vec{X} , in terms of the raw measurements, I_k .

3.1 First stage post-processing

The scheme we have described in Section 2.2 requires that a single horizontal of the scan consisted of 161 individual tests lasting two seconds each. At 50kS/s, there are 16.1 million data points in a single scan of the flame. The vast majority are data collected while the wire was passing uselessly through air, and the raw data are expressed as voltage versus time and not the wire current versus disc angle (which the above analysis requires).

Therefore, the first post processing step included four major activities

- 1. Apply the isoshunt's calibration to re-scale the voltage data into μA .
- 2. Use the photo interrupter's rising edge to translate time into disc angle for each measurement.
- 3. Organize the data into bins by disc angle so that all data at nearby disc angles are grouped together.
- 4. Produce statistics on each disc angle bin including number of data points, mean, median, and standard deviation.

The results were stored in text files and plotted (as in Figure 6 so they could be visually checked for anomalies. The bins were .0005 radians wide, and each usually contained 15 to 17 samples. Figure 6 shows a typical result from a single data set collected quite close to the torch tip. It is already evident that the method is sufficient to resolve important spatial details in the inner cones.

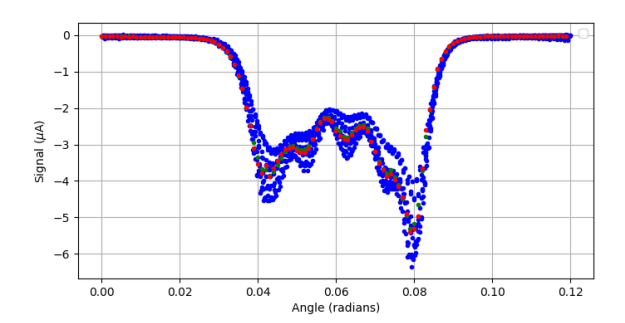


FIGURE 6. An example of the results of the first post-processing step.

3.2 Second-stage post-processing

Between the mean and median values produced in the first post-processing step, the median was found to offer superior rejection of intermittent asymmetrical jumps in the flame ion activity. Each median value was accumulated in a solution matrix using the formulation developed above. This process was repeated for each of the 161 files to accumulate a master solution matrix and vector defined in Equation 14.

A grid with 0.25mm (.01in) node spacing was selected. Finer resolution would have been impractical since the grid spacing is already equal to the wire diameter. Furthermore, as the grid resolution approaches the spacing between individual measurements, the solution matrix approaches singular. These settings were found to be a compromise between the desire for detailed resolution and numerical stability of the problem.

4 Results

Figures 7 show pseudo-color representations of the postprocessed wire current density in the flame. This indicator of the local concentration of ions depicts high densities of ions in the 12 inner cones that rapidly disperse into a uniform hollow cylinder. The ion density appears to be steadily in decline as the scanning height descends. In the coordinates shown, the disc is spinning counter-clock-wise in the plane of the page to the left of the flame.

To rule out the possibility of decreased signal to the wire due to corrosion or some other change in the wire's properties throughout these tests, they were conducted out-of-order; z = 3 mm, z = 6 mm, z = 4.5 mm, and z = 7.5 mm.

There are striped artifacts that appear along the *x*-axis behind the flame due to the unsteadiness in the flame that can be observed in Figure 6. The effect is readily understood by considering the explanation we offer for the transform in the introduction. When the wire is quite shallow in the flame, the signals are very weak. As the wire move deeper into the flame, the algorithm we have developed understands this increase in signal

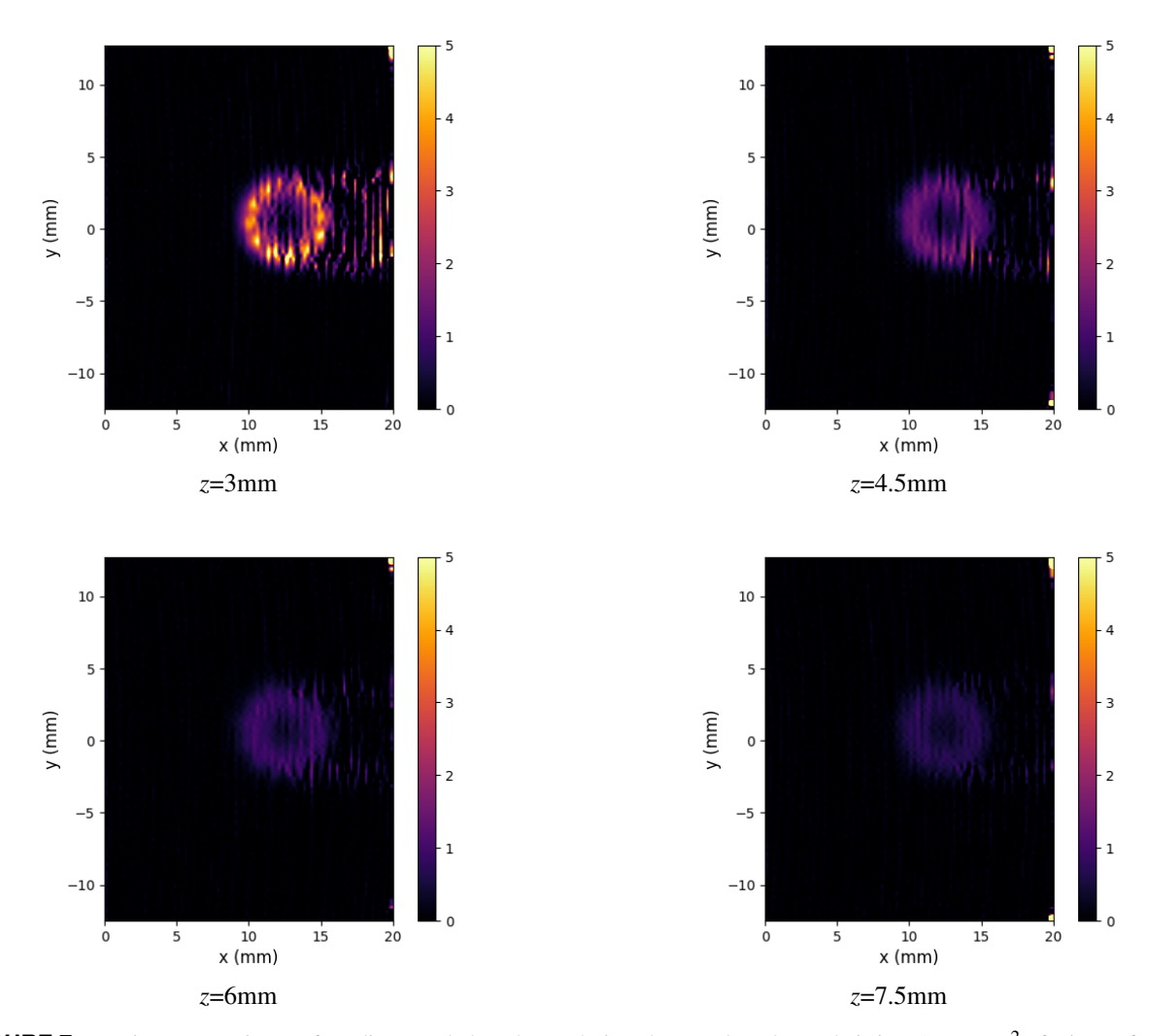


FIGURE 7. Ionic cross sections at four distances below the torch tip. The pseudo-color scale is in μ A per mm² of wire surface.

to be due to new signal encountered at the wire's tip. However, if the signal were to fluctuate due to natural oscillations in the flame, the algorithm would be erroneously assign the change to new signal encountered at the wire's tip. This causes intermittent stripes after the flame. Future efforts may endeavor to modify the system to quiet these oscillations.

It should be emphasized that we make no attempt to translate these to ion density measurements. Though this is entirely possible thanks to the work of Clements and Smy, there are a number of parameters (such as the local fluid velocity) that are not well known in our system. We will certainly perform this work, but for now, we merely assert that the ion density is proportional to the signal we have reported. Regions of the flame with very weak signal have very few ions and regions of the flame with strong signal have many ions.

5 Conclusions

The spinning disc Langmuir probe provides a valid method for collecting spatially resolved ion density measurements in a high-temperature atmospheric flame. This preliminary work validates the method that we will use to continue to study the electrical structure of the flame.

Even without translating these units into ion count per cubic mm, there are a number of important insights that can already be gained. Visual inspection of the luminous outer cone would place it closer to 10mm or more in diameter, but these data show no evidence of electrical charge so far from the centerline. Instead, charged particles seem to be tightly restricted to a ring roughly 6mm in diameter, directly downstream of the inner cones. There, their concentration appears to slowly decline.

There are a number of next steps that should be taken.

- 1. The Clements and Smy "frozen ion model" should be used to re-scale these data to estimates of ion concentration.
- 2. These measurements should be compared with computation fluid dynamics simulation.
- 3. These measurements should be used to develop a simplified one-dimensional model for the flame electrical properties.
- 4. The simulations should be compared against prior measurement (especially regimes 1 and 3).
- 5. Steps should be taken to quiet the flame oscillations.
- 6. These measurements should be repeated with various voltages applied to the torch.

Acknowledgements

The work presented here was made possible by award 1900698 from the National Science Foundation.

A Appendix

A.1 Interpolation

Each element is a finite domain in x, y space over which we may estimate the continuous function, J_D , at a point, $\vec{p} = [x, y]^T$, by linear interpolation of the node values.

$$J_D(\vec{p}) = X_{i,j} \phi_{00}(\vec{p}) + X_{i+1,j} \phi_{10}(\vec{p}) + \dots$$
$$X_{i,j+1} \phi_{01}(\vec{p}) + X_{i+1,j+1} \phi_{11}(\vec{p})$$
(15)

when the ϕ functions are interpolation functions which we must define. Note that this is only valid when \vec{p} lies within the element, so $x_i \le x \le x_{i+1}$ and $y_j \le y \le y_{j+1}$.

A formulation of the interpolation functions is facilitated by using a scaled coordinate system, $\hat{x} = (x - x_i)/(x_{i+1} - x_i)$, $\hat{y} = (y - y_j)/(y_{j+1} - y_j)$, or

$$[\hat{x}, \hat{y}]^T = \hat{\vec{p}} = \frac{\vec{p} - \vec{p}_{i,j}}{\delta},\tag{16}$$

This constitutes a coordinate system with its origin at the bottomleft most node in the element (node n or equivalently node i, j) extending to $\hat{x} = 1$ at its right-most, and $\hat{y} = 1$ at its top most extent. These interpolation functions are *only* valid in that range.

For the interpolated values for J_D to agree with the node values at the verticies, each interpolation function must be one at its own node and zero at the other three. This implies four constraints on each interpolation function, permitting a four-term x, y polynomial. Using the element-scaled coordinate system, the

resulting interpolation functions are

$$\phi_{00} = (1 - \hat{x})(1 - \hat{y}) \tag{17a}$$

$$\phi_{10} = \hat{x}(1 - \hat{y}) \tag{17b}$$

$$\phi_{01} = (1 - \hat{x})\hat{y} \tag{17c}$$

$$\phi_{11} = \hat{x}\hat{y} \tag{17d}$$

and may be more compactly written $\phi(\hat{p})$. Note that each ϕ is unity when \hat{p} is at its respective node, but declines to zero at all other nodes.

A.2 Line Segments

Constructing the wire's path in space and the bounds on an element's regime in space is accomplished by defining line segments. In the case of elements, the four segments defining their boundary are simply defined by the segments connecting the nodes. The wire may be imagined to extend a radius, *R*, from the center of rotation at some angle relative to the *x*-axis.

It is convenient to define a line segment by a starting point, \vec{p}_0 , and a direction, $\Delta \vec{p}$. Therefore, the line segment is defined as

$$\vec{p}(s) = \vec{p}_0 + s\Delta \vec{p} \qquad \forall s \in [0, 1]. \tag{18}$$

Negative values of s and values greater than 1 represented points projected beyond the bounds of the line segment. The value of s is related to the distance along the segment, r, by

$$r = s \|\Delta \vec{p}\|. \tag{19}$$

For line segments expressed within an element's dimensionless coordinate system,

$$\hat{\vec{p}}(s) = \frac{\vec{p}(s) - \vec{p}_n}{\delta} = \hat{\vec{p}}_0 + s\Delta\hat{\vec{p}}$$

$$\hat{\vec{p}}_0 = \frac{\vec{p}_0 - \vec{p}_n}{\delta}$$

$$\Delta\hat{\vec{p}} = \frac{\Delta\vec{p}}{\delta}.$$
(20)

This alternate formulation for a line segment is simply re-scaled by the elements size and offset by its bottom-left element's coordinates.

A.3 Calculating $\vec{\Lambda}$

Equation 14 reduces the problem to a matrix inversion in terms of sums of $\vec{\Lambda}_k = \vec{\Lambda}(R, d_k, \theta_k)$. Here, we use the interpolation functions to calculate $\vec{\Lambda}$ for the k data point with the disc center of rotation at $x = -d_k$, and the wire at an angle, θ_k . For each such wire location, elements may fall into three categories:

- 1. Elements through which the wire does not pass,
- 2. Elements with the wire passing through two faces,
- 3. An element with the wire passing through only one face.

The first will constitute the vast majority of elements for any given wire location and do not contribute to the integral. In this approach, we will consider each element that contains a segment of the wire, and we will accumulate their contributions to $\vec{\Lambda}$.

The integration of J_D over only the n element will contain contributions from the four nodes that form its limits,

$$\int_{(n)} J_D dr = X_{i,j} \int_{(n)} \phi_{00} dr + X_{i+1,j} \int_{(n)} \phi_{10} dr + \dots$$
$$X_{i,j+1} \int_{(n)} \phi_{01} dr + X_{i+1,j+1} \int_{(n)} \phi_{11} dr$$
(21)

Note that we have been quite deliberately vague with regard to the bounds on the integrals over r. Once we have isolated a line segment, $\vec{p}(s)$, within element n, each integral may be rescaled to be in terms of s,

$$\int_{(n)} \phi dr = \|\Delta \vec{p}\| \int_0^1 \phi(\hat{p}(s)) ds. \tag{22}$$

since $dr = \|\Delta \vec{p}\| ds$.

So, the four interpolation function integrals are

$$\Phi_{00} = \int_{0}^{1} \phi_{00}(s) ds = \int_{0}^{1} (1 - \hat{x}_{0} - s\Delta\hat{x})(1 - \hat{y}_{0} - s\Delta\hat{y}) ds
= \frac{\Delta\hat{x}\Delta\hat{y}}{3} - \frac{\Delta\hat{x}(1 - \hat{y}_{0})}{2} - \frac{\Delta\hat{y}(1 - \hat{x}_{0})}{2} + (1 - \hat{x}_{0})(1 - \hat{y}_{0})$$
(23a)

$$\Phi_{10} = \int_0^1 \phi_{10}(s) ds = \int_0^1 (\hat{x}_0 + s\Delta \hat{x}) (1 - \hat{y}_0 - s\Delta \hat{y}) ds
= -\frac{\Delta \hat{x} \Delta \hat{y}}{3} + \frac{\Delta \hat{x} (1 - \hat{y}_0)}{2} - \frac{\Delta \hat{y} \hat{x}_0}{2} + \hat{x}_0 (1 - \hat{y}_0)$$
(23b)

$$\Phi_{01} = \int_0^1 \phi_{01}(s) ds = \int_0^1 (1 - \hat{x}_0 - s\Delta \hat{x})(\hat{y}_0 + s\Delta \hat{y}) ds
= -\frac{\Delta \hat{x}\Delta \hat{y}}{3} - \frac{\Delta \hat{x}\hat{y}_0}{2} + \frac{\Delta \hat{y}(1 - \hat{x}_0)}{2} + (1 - \hat{x}_0)\hat{y}_0$$
(23c)

$$\Phi_{11} = \int_{0}^{1} \phi_{11}(s) ds = \int_{0}^{1} (\hat{x}_{0} + s\Delta\hat{x})(\hat{y}_{0} + s\Delta\hat{y}) ds
= \frac{\Delta\hat{x}\Delta\hat{y}}{3} + \frac{\Delta\hat{x}\hat{y}_{0}}{2} + \frac{\Delta\hat{y}x_{0}}{2} + \hat{x}_{0}\hat{y}_{0}$$
(23d)

Finally, we may construct $\vec{\Lambda}$ in terms of these Φ formulae.

Here, the contribution to each $\vec{\Lambda}$ element from only element *n* is

$$\Lambda_{i,j}^{(n)} = \|\Delta \vec{p}\| \Phi_{00} \tag{24a}$$

$$\Lambda_{i+1,j}^{(n)} = \|\Delta \vec{p}\| \Phi_{10} \tag{24b}$$

$$\Lambda_{i,j+1}^{(n)} = \|\Delta \vec{p}\| \Phi_{01} \tag{24c}$$

$$\Lambda_{i+1,j+1}^{(n)} = \|\Delta \vec{p}\| \Phi_{11}$$
 (24d)

and zero otherwise. The total $\vec{\Lambda}$ vector is constructed by summing these values contributed from all the elements.

$$\Lambda_{i,j} = \sum_{n} \Lambda_{i,j}^{(n)} \tag{25}$$

REFERENCES

- [1] Martin, C. R., Pond, T., Tomas, J., Schmit, J., Miguel, E., Untaroiu, A., and Xu, K., 2020. "Semiconductor aspects of the oxyfuel cutting torch preheat flame, part i: Measurements between torch and work". In Proceedings of the Manufacturing Science and Engineering Conference. Submitted.
- [2] Thompson, J. J., 1906. *Conduction of Electricity through Gases*, second ed. Cambridge University Press, London.
- [3] Langmuir, I., 1924. "Studies of electric discharges in gases at low pressures". *General Electric Review*, 27(12), p. 810.
- [4] Boucher, P. E., 1928. "The drop of potential at the cathode in flames". *Physical Review*, *31*, May.
- [5] Banta, H., 1929. "The mobility of positive ions in flames". *Physical Review,* 33, February.
- [6] Calcote, H. F., 1963. "Ion and electron profiles in flames". In Ninth Symposium on Combustion, Vol. 9, Combustion Institute, pp. 622–637.
- [7] MacLatchy, C. S., 1979. "Langmuir probe measurements of ion density in an atmospheric-pressure air-propane flame". *Combustion and Flame*, *36*, pp. 171–178.
- [8] Clements, R. M., and Smy, P. R., 1969. "Electrostatic-probe studies in a flame plasma". *Journal of Applied Physics*, *40*, pp. 4553–4558.
- [9] Clements, R. M., and Smy, P. R., 1970. "Ion current to a spherical probe in a flowing high-pressure plasma under thin-sheath conditions". *Proceedings of the IEE*, *117*(8), pp. 1721–1724.
- [10] Clements, R. M., and Smy, P. R., 1970. "Ion current from a collision-dominated flowing plasma to a cylindrical electrode surrounded by a thin sheath". *Journal of Applied Physics*, *41*(9), pp. 3745–3749.
- [11] Clements, R. M., and Smy, P. R., 1973. "Ion saturation currents to planar langmuir probes in a collision-dominated

flowing plasma". *Journal of Physics D: Applied Physics*, **6**, pp. 184–195.